Research Square

Preprints are preliminary reports that have not undergone peer review.
They should not be considered conclusive, used to inform clinical practice,
or referenced by the media as validated information.

Ultralow loss topological metamaterial in the visible spectrum

Jing Zhao
Medtronic plc, Boulder
Huan Chen
Northwestern Polytechnical University
Kun Song
Northwestern Polytechnical University
Liqin Xiang
Northwestern Polytechnical University
Qian Zhao
Tsinghua University
Chaohong Shang
Northwestern Polytechnical University
Xiaonong Wang
Northwestern Polytechnical University
Zhijie Shen
Northwestern Polytechnical University
Xianfeng Wu
Northwestern Polytechnical University
Yajie Hu
Northwestern Polytechnical University
xiaopeng zhao (xpzhao@nwpu.edu.cn)
Northwestern Polytechnical University

Article

Keywords: optical metamaterials, negative index metamaterials (NIMs)

Posted Date: March 18th, 2021

DOI: https://doi.org/10.21203/rs.3.rs-300159/v1

License: This work is licensed under a Creative Commons Attribution 4.0 International License.
Read Full License

Ultralow loss topological metamaterial in the visible spectrum

Jing Zhao[1]*, Huan Chen[2]*, Kun Song[2]*, Liqin Xiang[2], Qian Zhao[3], Chaohong Shang[2], Xiaonong Wang[2], Zhijie Shen[2], Xianfeng Wu[2], Yajie Hu[2] and Xiaopeng Zhao[2†]

[1]Medtronic plc, Boulder, CO 80301, USA.

[2]Smart Materials Laboratory, Department of Applied Physics, Northwestern Polytechnical University, Xi'an 710129 P. R. China.

[3]State Key Lab Tribology, Dept Mech Engn, Tsinghua University, Beijing 100084, P. R. China.

*These authors contributed equally to this work.

[†]Corresponding author. E-mail: xpzhao@nwpu.edu.cn.

Optical metamaterials give birth to the control and regulation of light. However, because of strong energy dissipation and fabrication difficulty in metals, low-loss isotropic three dimentional negative index metamaterials (NIMs) in the visible spectrum has long been regarded as an extremely challenging. Here we report an ultralow loss isotropic topological metamaterials for visible light. The ball-thorn-shaped meta-clusters with symmetrical structure consisting of dielectric and topological silver layer was proposed, the surface plasma resonance is formed inside a cluster unit with a height of two atomic layers, resulting in an optimized silver coating thickness about 1 nm. We invented a unique technique for preparing ultralow loss isotropic clusters and three-dimensional large area samples. The negative refractive index and the inverse Doppler effect of green and red light is measured by the prism method for the first time. This molecular crystals NIMs break through noble metal important energy losses and manufacturing difficulties.

Refraction of light is one of the basic phenomena in physics, the experimental verification of negative refraction embarked on a new wave of innovation in metamaterials[1–8]. Metamaterials are artificial media made of subwavelength metallic and dielectric periodic structure with properties that do not present in natural materials[4–6]. Metallic wires and split-rings (meta-atoms) were identified as building blocks to realize negative refraction by Pendry in his pioneering works[2,3]. Extraordinary electromagnetic properties in the microwave range associated with negative-index metamaterials (NIMs), including super-resolution lens[5], electromagnetic cloaking[6], inverse Doppler effect[7], and perfect absorber[8] have been reported over the last two decades.

Optical NIMs particularly in visible light make it possible to manipulate light at subwavelength scale[9,10]. Because of strong energy dissipation and significant fabrication difficulty in metals[11,12], low-loss isotropic three dimentional NIMs in the visible spectrum has long been regarded as a extremely challenging difficulty[13–15]. As a result, mainstream fabrication methods for optical metamaterials nowadays employ various etching techniques to forms meta-atoms[12], such as the double-fishnet structure[16,14] and the 3D wedge-shaped fishnet structure[13,17]. Much progress has been made in recent years with respect to developing bottom-up preparation approaches for metamaterials[18–21]. However, metamaterials based on the concept of noble metallic meta-atoms structure suffer from many inherent performance limitations including considerable ohmic loss, optical anisotropy, and difficulty in tuning[9,11]. The Mie resonances of dielectric particles provide a possible mechanism for realizing magnetic or electric resonance. Thanks to dielectric sphere's structure simplicity and isotropy, Mie resonance-based microwave metamaterials have already been realized in experimental settings[22,23], suggesting a promising direction for optical metamaterials[24,25]. Yet, this approach demands high permittivity for dielectric particles to generate strong resonant electromagnetic fields for loss minimization, resulting in a

practically difficult route to engineer isotropic infrared and visible light metamaterials. Metasurfaces that control light waves by introducing an abrupt phase shift at sub-wavelength scale have been proposed as an alternative approach[26,27]. Nevertheless, limited successes in the visible spectrum have been achieved to date[28,29]. Although plasmonic materials with a lower loss than noble metals have long been sought, the stable sodium-based plasmonic devices with state-of-the-art performance at near-infrared wavelengths was not available until quite recently [15].

The resonance is one of the intrinsic properties of metamaterials. Loss at the resonance frequency sometimes severely impairs metamaterial's extraordinary performance[9,10]. This problem becomes more prominent for the visible light because its skin depth is comparable to the thickness of metallic traces that are commonly found in a metamaterial unit cell[11,15]. Noble metals such as silver and gold are primary candidates for engineering frequency selective materials at optical frequencies. Published designs including the metal–dielectric–metal fishnet structures consist of a single functional layer along the direction of propagation[14,16], the 3D optical NIMs made of cascaded fishnet metamaterial[12,13,17] are all based on the meta-atoms which results in an optimal metal thickness of cell unit being about 20 to 50 nm. As a result, considerable loss is induced by volumetric currents and plasma resonances, making metamaterial properties much less attractive for meaningful applications. Up to this day, a significant scientific breakthrough in the visible zero-loss negative-index 3D isotropic metamaterials remain to be seen[9,15,25,28].

Here we theoretically and experimentally demonstrate the first ultralow loss isotropic topological metamaterials in the visible spectrum. The molecular crystals metamaterial of ball-thorn-shaped meta-clusters with symmetrical structure consisting of dielectric and topological silver layer have replaced the lithographically defined meta-atoms in existing NIMs, the surface plasma resonance can be formed inside a cluster unit with a height of two atomic layers, resulting

in an optimized silver coating thickness being about 1 nm. The unique technique for preparing ultralow loss isotropic clusters and three-dimensional large area samples by a bottom-up approach was invented. Using the prism method, we report the negative refractive index and the inverse Doppler effect of green and red light in experiment for the very first time. The proposed molecular crystal structure break through noble metal important energy losses and manufacturing difficulties, opening a door for assembling next-generation 3D molecular crystals NIMs devices of arbitrary shape despite their large physical size.

Design and behavior of the meta-clusters structure

Cells are the basic building blocks of all organisms (see Fig. 1a). Cilia, consisting of internal cytoplasm and surface plasmalemma, can be found on the surface of a cell. Cilia are known for their importance as the 'antennas' of a cell and their functions in terms of stimulating responses to surrounding environment, which include chemical sensation, signal transduction, and control of cell growth. Inspired by the ciliated cell structure, we created a ball-thorn-shaped metamaterial cluster (meta-cluster) model consists of a spherical kernel and many protruding rods (Fig. 1b) as analogous to the cilium-cell structure found in nature. Each ball-thorn-shaped unit is made of titanium dioxide (TiO_2) dielectric except for a thin layer of metal (topological silver) coating on the outer surface. Both the kernel and rods are made of TiO_2 coated by Ag of 1 nm in thickness. 600 identical rods with cross-sectional diameter of 15 nm are uniformly distributed around the surface of a kernel. l represents the diameter of the meta-cluster, r is the radius of the spherical kernel, and P refers to the lattice constant of the meta-cluster, the meta-cluster is fully immersed in polymethyl methacrylate (PMMA). The relative permittivity of Ag is set to be consistent with the actual Drude model value[30], of TiO_2 is 5.2 with a dissipation factor of 0.003, of PMMA is 2.5. This meta-cluster model is solved in Computer Simulation Technology (CST) Microwave Studio

(Supplementary Information S1). A peak in transmission coefficient indicates the meta-cluster resonates within the wavelength range of the red-light (Extended Data Fig. 1), a Mie resonance[22,31]. The effective parameters are numerically retrieved based on the Mie scattering theory[22, 31], which proves that the material composed of this structure is a metamaterial. At $\lambda = 645$ nm, the value of Re(n) reaches a minimum of −0.45 (Fig. 1c). The figure of merit (FOM) curve (in red) of the meta-cluster in the red-light band is shown in Fig.1d, where $FOM_{sim} = -Re(n)/Im(n)$ for $Re(n) < 0$, and Re(n) and Im(n) are the real and imaginary parts of the refractive index, respectively. FOM_{sim} arrives at a maximum of 10.3 at $\lambda = 623$ nm and is about 3.2 at $\lambda = 645$ nm where the value of Re(n) is the most negative. To achieve a similar effect in the green-light band, we reduced $l = 530$ nm, $r = 165$ nm, $P = 560$ nm. As expected, the transmission and reflection curves indeed reveals a Mie resonance at the green-light wavelengths (Extended Data Fig. 1). Similarly, the permeability, permittivity and refractive index of the meta-cluster are simultaneously negative at near 530 nm. At $\lambda = 538$ nm, the value of Re(n) reaches a minimum of −0.47 (Fig. 1c). The FOM curve (in green) of the green-light meta-cluster is shown in Fig. 1d. FOM_{sim} arrives at a maximum of 15.9 at $\lambda = 514.5$ nm and is about 2.2 at $\lambda=538$ nm where the value of Re(n) is the most negative.

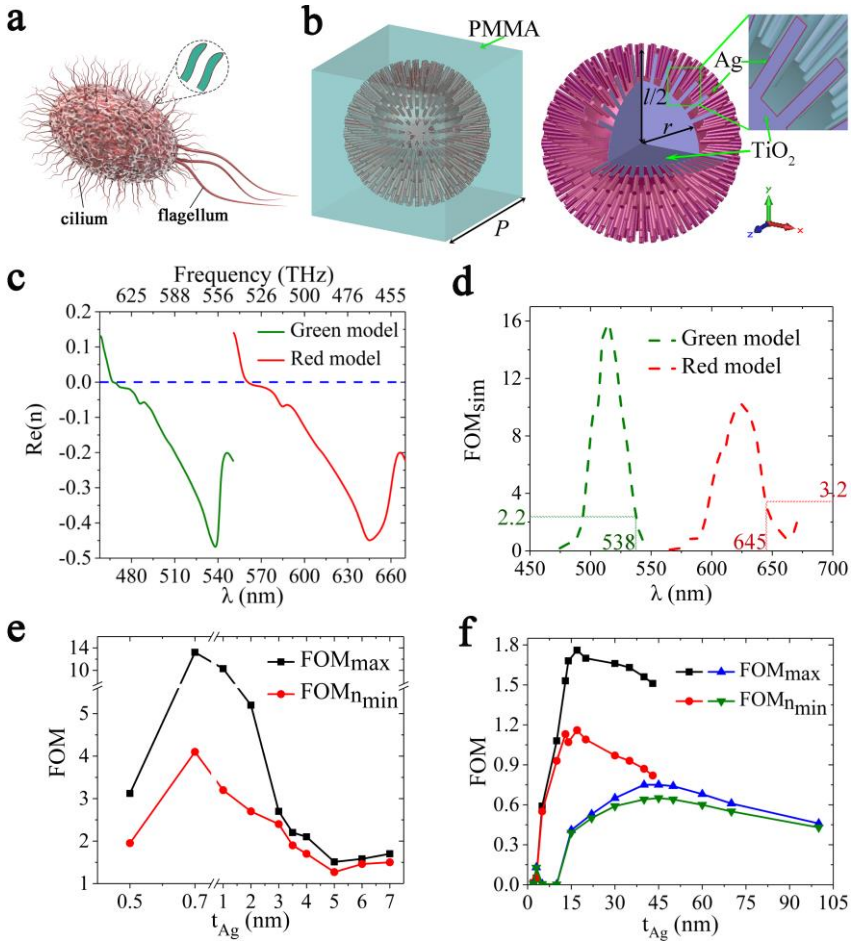

Fig. 1 | Behavior of the meta-cluster structure. a, Schematic of the biological cilium-cell. **b**, A meta-cluster model that mimics the cilium-cell structure consisting of a spherical kernel and lots of protruding rods. **c**, Effective refractive indices for the red-light meta-cluster (red line) with l = 640 nm, r = 215 nm, and P = 670 nm and the green-light meta-cluster (green line) with l = 530 nm, r = 165 nm, and P = 560 nm. **d**, FOM curves of the meta-clusters resonating at the red-light (red dotted line) and green-light (green dotted line), respectively. **e**, FOM of the red-light meta-cluster structure as a function of Ag layer thickness t_{Ag}. **f**, FOMs of fishnet structures at different Ag layer thickness. Black square and red circle lines represents the results obtained using the Ag-Al_2O_3-Ag fishnet structure whose geometrical parameters refer to the published work[14] and blue triangle and green inverted-triangle lines represents the results obtained using the Ag-MgF_2-Ag fishnet structure whose geometrical parameters refer to the published work[17].

Based on effect of Ag layer thickness t_{Ag} on the response behavior of the red-light meta-cluster in PMMA medium (Extended Data Fig. 2), Fig. 1e shows the relationship between metal film thickness and FOM variation. It can be seen that with silver as resonant material, the plasma resonance can be formed with a height of only two atomic layers, resulting in an optimized silver

coating thickness being about 1 nm. However, in the models of meta-atom cell unit, such as double fishing nets[16,17] or nanowires[21], the optimal metal film thickness of the unit is 20–50 nm (Fig. 1f). Our cluster design is independent of the previously widely used meta-atom cell design philosophy. This model greatly reduces the silver coating thickness required for achieving high FOM, the resulting FOM is nearly an order of magnitude greater than the state-of-arts. It is indeed this molecular crystals NIMs significant reduction in silver coating thickness that provides the physical basis for the decreased joule heating and thus the realization of ultra-low losses. It breaks through the dilemma of whether to use noble metals in engineering visible light meta-atom NIMs. In addition, spherically symmetric cluster units directly solve the anisotropy problem of cell structure.

Preparation and characterization of meta-cluster particles

The Ag/AgCl/TiO_2@PMMA meta-cluster particles corresponding to red-light and green-light are prepared using the solvothermal synthesis method (see Methods). In order to solve the problem of the coating of nano-silver layer of ball-thorn-shaped clusters, AgCl is firstly formed by mixing a certain amount of $AgNO_3$ into $TiCl_4$ during the process of preparing the TiO_2 rods. After a photoreduction method, AgCl further disintegrates into elemental chlorine and metallic silver. The latter precipitates on the outer surface of the ball-thorn-shaped structure to form the topological silver distribution about 1 nm coating. The ball-thorn-shaped particle is shown in the scanning electron microscope (SEM) image (Fig. 2a). Next, these agglomerated particles are immersed in PMMA and illuminated to form the Ag/AgCl/TiO_2@PMMA particles (Fig. 2b). Figure 2c shows the TEM images of the particles that resonate in the green (left) and red (right) light spectrum, revealing a classic kernel (AgCl/TiO_2) – shell (PMMA) structure. A high-magnification view in Fig. 2d confirms the presence of PMMA filling between different nanorods. Another high-magnification TEM image of an individual nanorod shows a rather rough outer surface (Fig. 2e),

which is possibly a result of the precipitation of Ag nanoparticles. X-ray diffraction (XRD) patterns (Fig. 2f) suggests that some AgCl crystals have decomposed into elemental Ag and chlorine, and thus the ultimate post-illumination nanostructure should be Ag/AgCl/TiO_2@PMMA (Extended Data Fig. 3). Ultraviolet-visible-near infrared (UV-VIS-NIR) absorption spectra of the AgCl/TiO_2 particles, AgCl/TiO_2@PMMA particles with no illumination and illuminated AgCl/TiO_2@PMMA particles (i.e., Ag/AgCl/TiO_2@PMMA particles) are plotted in Fig. 2g. AgCl/TiO_2 particles only absorb ultraviolet light (i.e., $\lambda < 410$ nm). Similar absorption characteristic at ultraviolet light wavelengths is seen for the AgCl/TiO_2@PMMA particles without going through any illumination (except for a slower varying and slightly reduced magnitude thanks to the PMMA coating). However, after illumination, noticeable difference in absorption is found in the visible light range for the AgCl/TiO_2@PMMA particles. These illuminated AgCl/TiO_2@PMMA particles not only exhibit intrinsic absorption behavior of AgCl/TiO_2 at ultraviolet light wavelengths, but also achieve a wideband absorption in the visible spectrum. Recall the evidence from previous XRD analysis, the increased absorption appeared in the visible light band is likely due to the local plasmon resonance (LPR) of the precipitated Ag nanoparticles. It is concluded that the composition of the post-illumination particles is Ag/AgCl/TiO_2@PMMA, electron microscope analysis shows that topological silver distribution with a thickness of about 1nm can be formed (Extended Data Fig. 3). Note that conventional cell units, such as fish nets and nanowires, are spatially asymmetric, greatly limiting the possibility for self-assembly. On contrary our meta-clusters are spherically symmetric, making them perfect candidates for self-assembly.

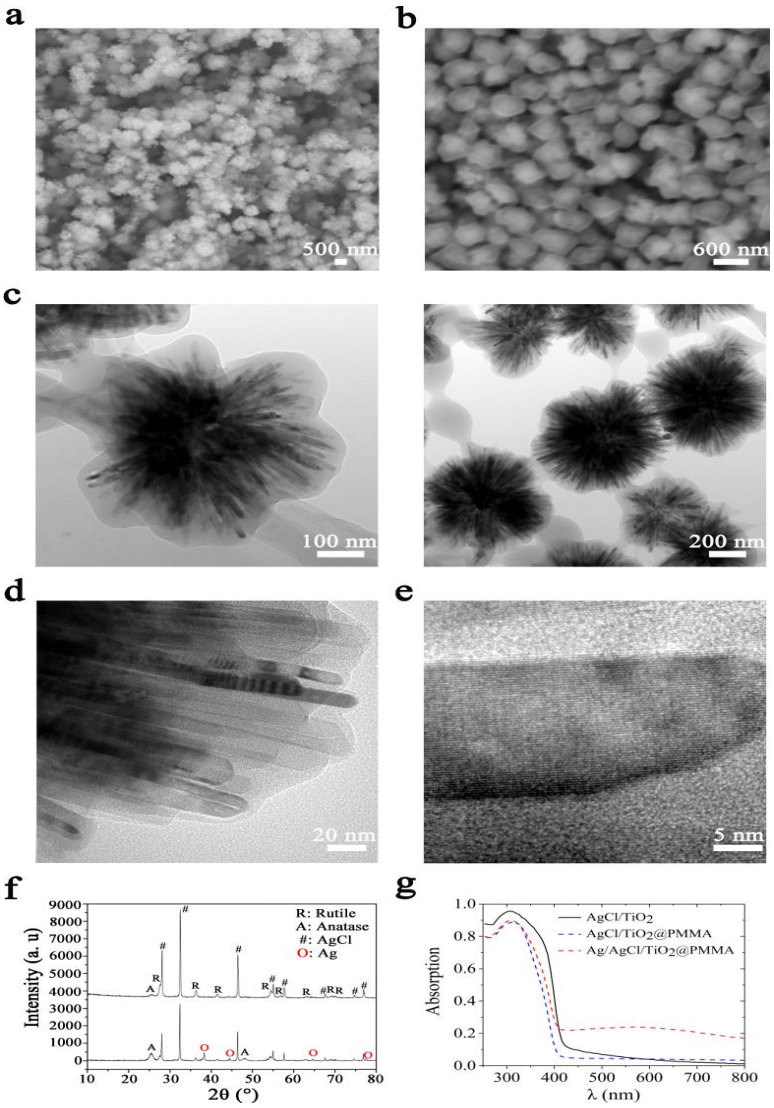

Fig. 2 | Morphology and characterization of the Ag/AgCl/TiO_2@PMMA particles. SEM images of AgCl/TiO_2 particles **a**, Ag/AgCl/TiO_2@PMMA particles **b**. **c**, **d**, TEM images of Ag/AgCl/TiO_2@PMMA particles: **c**, field of view of green-light (left) and red-light (right) particles; **d**, regional view of a composite particle, which is made of a ball-thorn-shaped inorganic kernel and a thin transparent organic PMMA shell. **e**, A high magnification TEM image of a protruding nanorod, Color variation indicates different chemical compositions. **f**, XRD patterns of the AgCl/TiO_2@PMMA (top) and Ag/AgCl/TiO_2@PMMA (bottom) particles. After the particles being photoreduction, in addition to the peaks associated with TiO_2 and AgCl crystals, local maximums of varying intensities (red hollow circles) at 38.3°, 44.4°, 64.6°, and 77.5°—corresponding to the respective (111), (200), (220), and (311) crystal faces of Ag—appeared in the bottom spectral line. **g**, UV-VIS-NIR absorption spectra of AgCl/TiO_2 (solid black line), AgCl/TiO_2@PMMA (blue dashed line) and Ag/AgCl/TiO_2@PMMA particles (red dashed line).

Negative refraction in the visible spectrum

Red-light and green-light 3D wedge-shaped metamaterial samples were fabricated by assembling the Ag/AgCl/TiO_2@PMMA particles of different sizes (see Methods, Supplementary Fig. S5, S6 , and Table S1). The ~1° wedge-shaped sample is 5 mm in width, 1 mm in length, and 20 μm in thickness—which is about the height of 30 vertically stacked layers of Ag/AgCl/TiO_2@PMMA particles (Fig. 3a).

Using the method proposed in ref. 11, we designed our own experiment (see Supplementary Fig. S7). Measured refractive indices (see Supplementary Fig. S8, S9 and Table S2, S3) of the green-light sample G, the red-light sample R, and the control sample assembled by TiO_2@PMMA particles are plotted in Fig. 3c. The negative refraction for sample R occurs at around 610–640 nm, and the minimum refractive index is –0.41 at 630 nm; the negative refraction for sample G occurs at around 520–550 nm, and the minimum refractive index is about –0.30 at 532 nm. These two measured refractive indices are in a reasonably good agreement with the simulation results (Fig. 1d, g). Measured refractive index $S_{TiO2@PMMA}$ of the TiO_2@PMMA sample remains nearly unchanged around a value of 2.2 – close to that of anatase – throughout the visible spectrum, the result of this control sample validates the accuracy of our measurement system. Furthermore, it also demonstrates that the negative refraction observed in the sample R and G indeed originates from the LPR of the topological silver nanoparticles residing on the outer surface of the ball-thorn-particles (consistent with the characterization in Fig. 2e, f, g).

The figure of merit $FOM_{exp'}$ ($= -\mathrm{Re}(n_{exp})/\mathrm{Im}(n)_{sim}$ for $n_{exp}<0$, and $\mathrm{Im}(n)_{sim}$ are the imaginary parts of the refractive index obtained by numerical simulation of the meta-clusters) is plotted in Fig. 3d. It is worth noting that $FOM_{exp'}$ (≈ 4.3 at $\lambda = 532$ nm and 12.8 at $\lambda = 630$ nm) is greater than FOM_{sim} predicted by simulation, which is about 2.2 at $\lambda = 538$ nm and about 3.2 at $\lambda = 645$ nm where the value of Re(n) is the most negative (Fig. 1e). This is because we assumed a uniformly

distributed Ag layer of 1 nm in thickness when constructing the meta-cluster model in simulation. However, as proven by the TEM images (Fig. 2e and Extended Data Fig. 3b), coverage of the Ag layer on the outer surface of the particles is topological distribution. Less metal presence in the resonance structure likely leads to a reduction in transmission loss caused by volumetric current and plasma resonance.

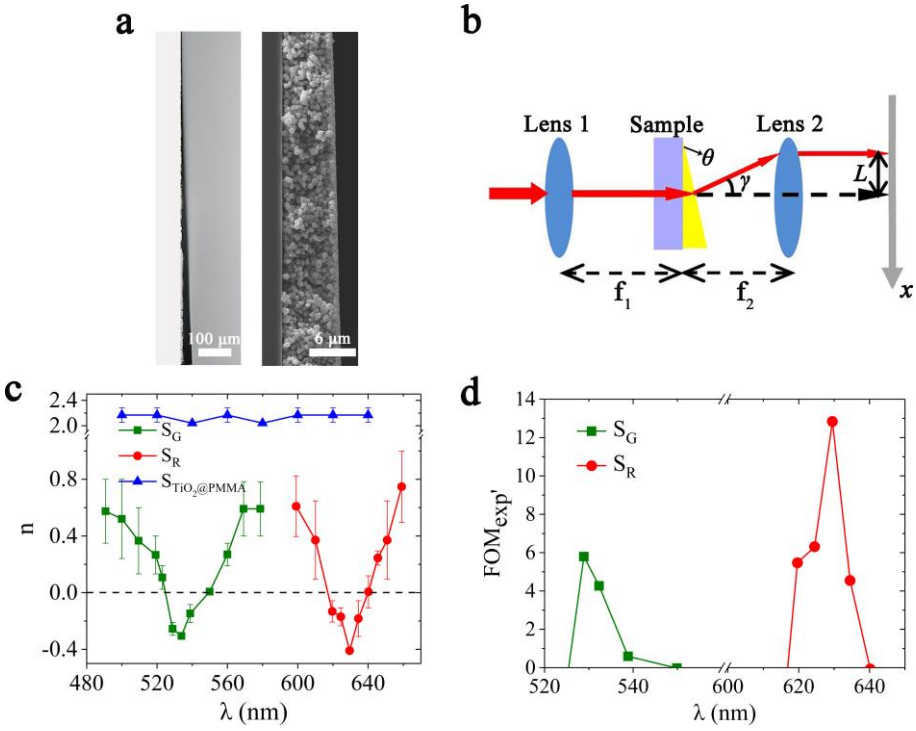

Fig. 3 | Characterization and measurement of the 3D wedge-shaped samples. **a**, Microscopic (left) and SEM (right) images of the wedge-shaped metamaterial sample (side view). **b**, Schematic of negative refraction measurement. θ represents the wedge angle of the prepared 3D wedge-shaped sample. γ refers to the angle between the outgoing beam and the extension line of the incoming beam. L represents the offset of the refracted spot in x-axis. $f_1 = f_2 = 12.7$ mm are the focal lengths of lenses 1 and 2, respectively. **c**, Measured refractive indices of the green-light sample G, the red-light sample R, and the control sample assembled by TiO_2@PMMA particles. **d**, FOM_{exp}' curves of samples G and R at green-light and red-light wavelengths, respectively.

There are direct and indirect methods to test negative refraction in experiments (Extended Data Table 1).The direct prism test method requires large 3D wedge samples, because of the inevitable

cost of high resistive loss, the best result in literature to date is obtained in the infrared band λ = 1.76 μm[13]. For the first time, we measured the refractive index of a metamaterial sample at red and green light frequencies using a direct method. Our ultra-low loss, isotropic and three-dimensional large-surface-area samples essentially enabled a successful prism measurement.

Inverse Doppler Effect of metamaterials in visible spectrum

Doppler effect refers to the change of frequency of a wave received by an observer with respect to the wave source when there is a relative movement between each other. It has been widely used in celestial mechanics, medical diagnosis, weather and aviation radar system and many other scientific and engineering fields. Veselago[1] theoretically predicted the existence of inverse Doppler effect in negative refractive index materials. Seddon[7] indirectly realized an inverse Doppler effect at 1−2 GHz using a magnetic nonlinear transmission line for the first time in experiment. Chen *et al.*[8] observed inverse Doppler effect in the infrared spectrum (λ = 10.6 μm) for the first time by using the two dimensional photonic prism composed of Silicon rods. Recently Shi *et al.* predicted and demonstrated inverse Doppler effect specific to the Vavilov-Cherenkov cone scenario in a uniform positive refractive index medium[32]. High loss, anisotropy and difficulties in fabricating three-dimensional metamaterials with large areas make experimental observation of inverse Doppler effect in visible spectrum a great challenge that has not been broken through to date.

Because the frequency of light is too high to be measured directly, Doppler effect is usually measured by optical heterodyne interferometry[8]. According to the method in ref. 8, we designed a high-precision laser heterodyne detection system based on the refraction of a visible laser beam through the prepared metamaterial wedge-shaped sample (Fig. 4a). Uniform change in optical path

when light passing through a moving medium results in an observable inverse Doppler effect in visible spectrum (Supplementary Information S4).

The negative refractive index material used for Doppler effect measurement was the ball-thorn shaped Ag/AgCl/TiO_2@PMMA. To satisfy the width requirement for refractive laser Doppler effect measurement, we prepared two wedge-shaped samples resonating at green light wavelength 525 nm and red light wavelength 632 nm (the bottom size is 5 mm×2 mm, hence the allowed distance of movement is 2 mm for the laser beam), denoted as sample Gc and sample Rc respectively. We sent one laser light with a wavelength of 532 nm through the sample Gc (wedge angle θ =1.7, refractive index n = –0.3) and another laser light with a wavelength of 632.8 nm through the sample Rc (wedge angle θ = 1.4, refractive index n = –0.41).

Fig. 4b shows the beat frequency of sample Rc at different velocities and the Doppler frequency shift inside the sample. The beat frequency value Δf in the graph is obtained by fast Fourier transform of the corresponding signal recorded by the detector. These measured values are in a reasonably good agreement with the theoretical predictions. The experiment was carried out at a sample velocity from 20 μm/s to 200 μm/s with a step size of 20 μm/s. We can clearly see that at these speeds, all Doppler shift values $(f_1 - f_0)k$ for the measured samples are positive, implying the occurrence of inverse Doppler effect. We also observed a similar effect by using sample Gc as shown in Fig. 4c.

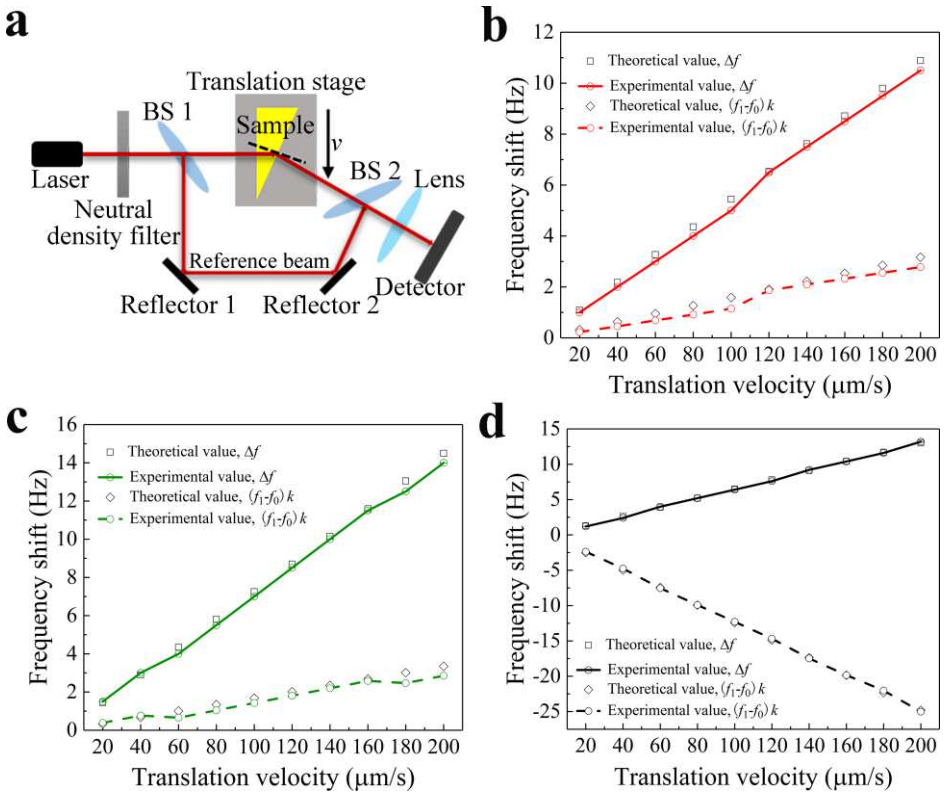

Fig. 4 | Doppler effect measurement. **a**, Schematic diagram of Doppler effect heterodyne detection system. **b**, **c**, **d**, Beat frequency Δf and Doppler frequency shift $(f_1 - f_0)k$ of Doppler effect observed at different velocities for sample Rc, sample Gc, and TiO_2@PMMA sample, respectively.

Fig. 4d shows the beat frequency and Doppler frequency shift of the measured TiO_2@PMMA wedge sample at different velocities. It can be seen that all the Doppler frequency shifts $(f_1 - f_0)k$ are negative and close to the theoretical values. According to the analysis (Supplementary Information S4), when the source is moving away from the receiver, the Doppler frequency shift value $(f_1 - f_0)k$ in the sample should be negative, implying red shift in a normal Doppler effect. This result not only demonstrates the feasibility of measuring Doppler effect using a wedge sample but also suggests that our measurement systems is capable of distinguishing inverse Doppler effect from normal Doppler effect. Doppler effect is one of the most basic mechanisms in physics and has wide applications in various fields. This ultralow loss, isotropic, 3D large size metamaterial

sample prepared using our novel fabrication method confirms the inverse Doppler effect in the visible spectrum for the very first time, which forms a solid foundation for its future application.

In summary, we have demonstrated an ultralow loss molecular crystals NIMs in the visible spectrum. The phenomenon of surface plasmon resonance excited by topological silver layer of ball-thorn-shaped meta-clusters was found, which broke through the dilemma of high loss of noble metal meta-atom NIMs. A cluster material and a three-dimensional large area sample preparation method are proposed. The negative refraction is measured by prism direct measurement at green and red-light wavelengths. Inverse Doppler effects of red and green light were measured for the first time by interferometry. The topological silver layer minimizes the resistance loss of the constituent noble metal at optical frequency and prevents a large block of metamaterials from being opaque. Importantly, our isotropic meta-clusters provide an assembling method for next-generation NIMs devices of arbitrary shape despite their large physical size, opening the door to the ideal NIMs[10]. Although our demonstration was carried out in the visible range, the design principles should be generalizable to other frequency regimes, such as terahertz and infrared frequencies. Lastly, since propagating waves with large wave vectors, which are evanescent in air or dielectrics, are supported in this type of low loss metamaterials, manipulating visible light at subwavelength scale may become possible[11]. This paves the way for a host of emerging technologies such as optical cloaking[6], optical optical plasmonic devices[15].

References

1. Veselago, V. G. The electrodynamics of substances with simultaneously negative values of permittivity and permeability. *Sov. Phys. Usp.* 10, 509–514 (1968).
2. Pendry, J. B., Holden, A. J., Stewart, W. J. & Youngs, I. Extremely low frequency plasmons in metallic mesostructures. *Phys. Rev. Lett.* 76, 4773–4776 (1996).
3. Pendry, J. B., Holden, A. J., Robbins, D. J. & Stewart, W. J. Magnetism from conductors and enhanced nonlinear phenomena. *IEEE Trans. Microwave Theory Tech.* 47, 2075–2084 (1999).
4. Shelby, R. A., Smith, D. R. & Schultz, S., Experimental verification of a negative index of refraction. *Science* 292, 77–79 (2001).
5. Zhang, X. & Liu, Z. Superlenses to overcome the diffraction limit. *Nat. Mater.* 7, 435–441 (2008).
6. Ergin, T., Stenger, N., Brenner, P., Pendry, J. B. & Wegener, M. Three-dimensional invisibility cloak at optical wavelengths. *Science* 328, 337–339 (2010).
7. Seddon, N. & Bearpark, T. Observation of the inverse Doppler effect. *Science* 302, 1537–1540 (2003).
8. Chen, J. B. *et al.* Observation of the inverse Doppler effect in negative-index materials at optical frequencies. *Nature Photon.* 5, 239–242 (2011).
9. Shalaev, V. M. Optical negative-index metamaterials. *Nat. Photon*. 1, 41–48 (2007).
10. Soukoulis, C. M. & Wegener, M. Optical metamaterials—more bulky and less lossy. *Science* 330, 1633–1634 (2010)
11. Soukoulis, C. M. & Wegener, M. Past achievements and future challenges in the development of three dimensional photonic metamaterials. *Nat. Photon.* 5, 523–530 (2011).
12. Tseng, M. L. *et al.* Fabrication of multilayer metamaterials by femtosecond laser‐induced forward‐transfer technique. *Laser Photonics Rev.* 6, 702–707 (2012).
13. Valentine, J. *et al.* Three-dimensional optical metamaterial with a negative refractive index. *Nature* 455, 376 (2008).
14. Xiao, S. M., Chettiar, U. K., Kildishev, A. V., Drachev, V. P. & Shalaev, V. M. Yellow-light negative-index metamaterials. *Opt. Lett.* 34, 3478–3480 (2009).
15. Yang, W. *et al.* Stable, high-performance sodium-based plasmonic devices in the near infrared. *Nature* 581, 401-405 (2020).
16. Dolling, G., Wegener, M., Soukoulis, C. M. & Linden, S. Negative-index metamaterial at 780 nm wavelength. *Opt. Lett.* 32, 53–55 (2007).
17. Liang, Y., Yu, Z., Ruan, N., Sun, Q. & Xu, T. Freestanding optical negative-index metamaterials of green light. *Opt. Lett.* 42, 3239–3242 (2017).
18. Liu, H., Zhao, X., Yang, Y., Li, Q. & Lv, J. Fabrication of infrared left‐handed metamaterials via double template‐assisted electrochemical deposition. *Adv. Mater.* 20, 2050–2054 (2008).
19. Vignolini, S. *et al.* A 3D optical metamaterial made by self‐assembly. *Adv. Mater.* 24, OP23–OP27 (2012).

20. Gómez-Castaño, M. *et al.* Electrodeposited negative index metamaterials with visible and near infrared response. *Adv. Opt. Mater.* 2000865 (2020).
21. Yao, J. *et al.* Optical negative refraction in bulk metamaterials of nanowires. *Science* 321, 930–930 (2008).
22. Zhao, Q. *et al.* Experimental demonstration of isotropic negative permeability in a three-dimensional dielectric composite. *Phys. Rev. Lett.* 101, 027402 (2008).
23. Zhao, Q. *et al.* Tailorable zero-phase delay of subwavelength particles toward miniaturized wave manipulation devices. *Adv. Mater.* 27, 6187–6194 (2015).
24. Moitra, P. *et al.* Realization of an all-dielectric zero-index optical metamaterial. *Nat. Photon.* 7, 10 791–795 (2013).
25. Limonov, M. F., Rybin, M. V., Poddubny, A. N. & Kivshar, Y. S. Fano resonances in photonics. *Nat. Photon.* 11, 543–554 (2017).
26. Yu, N. *et al.* Light propagation with phase discontinuities: generalized laws of reflection and refraction. *Science* 334, 333 (2011).
27. Yu, N. & Capasso, F. Flat optics with designer metasurfaces. *Nat. Mater.* 13, 139–150 (2014).
28. High, A. A. *et al.* Visible-frequency hyperbolic metasurface. *Nature* 522, 192–196 (2015).
29. Li, S. Q. *et al.* Phase-only transmissive spatial light modulator based on tunable dielectric metasurface. *Science* 364, 1087–1090 (2019).
30. Johnson, P. B. & Christy, R. W. Optical constants of the noble metals. *Phys. Rev. B* 6, 4370–4379 (1972).
31. Mie, G. Beiträge zur Optik trüber Medien, speziell kolloidaler Metallösungen. *Annalen der physik* 330, 377–445 (1908). 30
32. Shi, X. *et al.* Superlight inverse Doppler effect. *Nat. Phys.* 14, 1001–1005 (2018).

Methods

Preparation of the meta-cluster particles. *First, Ball-thorn-shaped $AgCl/TiO_2$ particles preparation.* The titanium tetrachloride ($TiCl_4$) is added dropwise to deionized water (analytical reagent) under ice bath to prepare a 38.5 wt% solution. The silver nitrate ($AgNO_3$, analytical reagent) is dissolved in deionized water to prepare a solution with a concentration of 0.0395 g/mL. The $AgNO_3$ solution is added to the tetrabutyl titanate (TBT) and toluene mixture and stirred for 30 min. A certain amount of $TiCl_4$ solution is also added and stirred for 1 h. The mixture is transferred to a Teflon-lined autoclave. The reactor is placed in a constant-temperature drying oven

(101A-1E) at 150°C for 24 h. The obtained product is washed several times with absolute ethanol (EtOH, analytical reagent), and then dispersed in ethanol for use or filtered and air-dried to obtain $AgCl/TiO_2$ particles. 1.7–2 mL of $TiCl_4$ solution is added when preparing the red-light particles, and 1.3–1.5 mL of $TiCl_4$ solution is added when preparing the green-light particles.

Second, Functionalization of $AgCl/TiO_2$ particles. A certain amount of the prepared $AgCl/TiO_2$ particles are added into the EtOH to obtain a 50-mL suspension. The suspension is then transferred into a 100-mL three-necked flask and stirred at 90 rpm for 30 min. 2 mL of polyethylene glycol-400 (PEG-400, analytical reagent) is dissolved in 5 mL of EtOH and slowly dropped in the three-necked flask. After stirring the suspension for 1 h, 1 mL of γ-methacryloxy propyltrimethoxy silane (MPS, analytical reagent) is dissolved in 5 mL of EtOH and slowly added into the three-necked flask. Similarly, after stirring the suspension again for 5 h, 1 mL of ammonium hydroxide (25 wt%) is dissolved in 5 mL of EtOH and slowly dropped into the three-necked flask. After being stirred for 10 h, the suspension is centrifuged at a rate of 2200 rpm for 3 min to discard the supernatant. The procedure is repeated 2 to 3 times, the precipitated MPS-functionalized $AgCl/TiO_2$ particles are obtained.

Third, PMMA-coated $AgCl/TiO_2$ particles ($AgCl/TiO_2$@PMMA). The $AgCl/TiO_2$@PMMA composite particles were synthesized by the route that the monomer was adsorbed onto the modified $AgCl/TiO_2$ followed by dispersion polymerization. A certain amount of the functionalized $AgCl/TiO_2$ particles is transferred to a 250 mL three-necked flask. 2 mL of methyl methacrylate (MMA, analytical reagent) and 10 μL of ethylene glycol dimethacrylate (EGDMA, analytical reagent) are dissolved in 25 mL of EtOH. The mixture is then slowly dropped in the three-necked flask. After stirring the suspension in the three-necked flask at 90 rpm for 1 h, 0.2 g of polyvinyl pyrrolidone (PVP, analytical reagent) is dissolved in 80 mL of deionized water and

added to the three-necked flask using a funnel. The suspension is continuously stirred for 1 h, and the three-necked flask is transferred to a thermostat water bath (80°C) and condensed with nitrogen. Subsequently, 0.06 g of kalium persulfate (KPS, analytical reagent) is dissolved in 6 mL of deionized water. Under constant stirring, 6 mL of KPS solution is added to the three-necked flask in three portions: 2 mL is dropped every 2 h. After the last addition of the KPS solution, the suspension is stirred for 6 h to complete the coating of $AgCl/TiO_2$ and obtain a suspension of $AgCl/TiO_2$@PMMA particles. The resulting suspension is centrifuged at 3000 rpm for 5 min to discard the supernatant. The remaining precipitate is then washed with the deionized water and centrifuged for several times. The final precipitate is washed with a small amount of deionized water before transferring to a 10 mL vial for storage.

Finally, Ag/AgCl/TiO₂@PMMA composite particles. The quartz glass is hydrophilically treated. The clean quartz glass (1 cm × 2 cm) is sonicated in alcohol for 30 min, washed with deionized water, and then boiled for 1 h in a mixture of 30% hydrogen peroxide (H_2O_2, analytical reagent) and deionized water (7:3 by volume). The suspension of the $AgCl/TiO_2$@PMMA particles is spin-coated onto a hydrophilically treated glass substrate using a spin coater. Finally, the glass substrate coated with $AgCl/TiO_2$@PMMA particles is placed a photoreduction process under an incandescent lamp (or a xenon lamp, $\lambda > 420$ nm) for 10 h. Part of AgCl in the particles is decomposed into Ag elementary substance, which is precipitated on the surface of the particles to obtain $Ag/AgCl/TiO_2$@PMMA particles.

Characterization. The morphology was observed by scanning electron microscopy (SEM, JSM-6700) and transmission electron microscopy (TEM, JEOL-3010). The crystal structure was characterized by the powder X-ray diffraction (XRD, Philips X'Pert Pro) with CuK_α irradiation

(40kV/35mA) and step size of 0.033° in the 2θ range of 10°~80°. Absorbance spectra were measured using UV-VIS-NIR spectrophotometer (HITACHI U-4100).

Preparation of 3D wedge-shaped samples. A gravity self-assembly device (Supplementary Fig. S5) is set as a platform to prepare the wedge-shaped sample. The lifting slab of the experiment platform is adjusted to be horizontal. The 5 mm × 10 mm glass strip is horizontally positioned in the glass substrate, whereas another hydrophilically treated glass strip (20 mm × 40 mm) is vertically placed on the glass strip (5 mm × 10 mm) and pressed down with a proper force to ensure that the suspension will not leak during the painting. Nearly 3.5 μL of the suspension is collected using a pipette and evenly painted from one end to the other along the corner between the two orthogonal glass strips. Under the action of hydrophilicity and gravity, a wedge-shaped suspension is formed. After the water in the wedge-shaped suspension evaporates at room temperature, the horizontal glass strip containing the wedge-shaped sample with Ag/AgCl/TiO_2@PMMA particles is taken down.

Measurement of the refractive index. The diagram of the experimental setup is displayed in Supplementary Fig. S7. The refractive index of the wedge-shaped sample at different incident wavelengths is obtained in accordance with the following formula by changing the incident wavelength and repeating the measurement:

$$n=\sin\{[\arctan(0.625L/f_2)+\theta]\}/\sin(\theta),$$

where L is the displacement of the refracted spot, f_2 is the distance from lens 2 to the sample, that is, the focal length of lens 2, and θ is the wedge angle of sample.

Numerical simulations. The boundary conditions of the model are set as Perfect Electric Conductor (PEC) in the *x* direction, Perfect Magnetic Conductor (PMC) in the *y* direction, and Open in the *z* direction which is also the direction of the incident light beam. This meta-cluster unit cell model is then solved using the time domain solver in CST Microwave Studio. Based on the Mie theory, the effective parameters are retrieved from the simulation results. The retrieve method is introduced in the Supplementary Information S1.

Data availability

The data that support the findings of this study are available from the corresponding author on reasonable request.

33. Xiao, S. *et al.* Loss-free and active optical negative-index metamaterials. *Nature* **466**, 735–738 (2010).
34. Chettiar, U. K. *et al.* Dual-band negative index metamaterial: double-negative at 813 nm and single-negative at 772 nm. *Opt. Lett.* **32**, 1671–1673 (2007).
35. Garcia-Meca, C. *et al.* Low-loss multilayered metamaterial exhibiting a negative index of refraction at visible wavelengths. *Phys. Rev. Lett.* **106**, 067402 (2011).
36. Jen, Y. J., Chen, C. H. & Yu, C. W. Deposited metamaterial thin film with negative refractive index and permeability in the visible regime. *Opt. Lett.* **36**, 1014–1016 (2011).

Acknowledgements

This work was supported by the National Natural Science Foundation of China (Grant Nos. 11674267, 51272215).

Author Contributions

J.Z and X.Z conceived the idea and designed the model, H.C., K.S., J.Z and Q.Z performed the simulation study. L.X., C.S and X.W performed the preparation and characterization of the meta-cluster structure sample, X.Z., Z.S., X.W and Y.H performed the optical experiments. X.Z., J.Z.

and H.C. drafted the text, aggregated the figures, and wrote the paper with input from all co-authors, X.Z and J.Z discussed the results and revised the manuscript.

Competing interests

The authors declare no competing interests.

Additional information

Extended data is available for this paper.

Supplementary Information is available for this paper.

Correspondence and requests for materials should be addressed to X.Z.

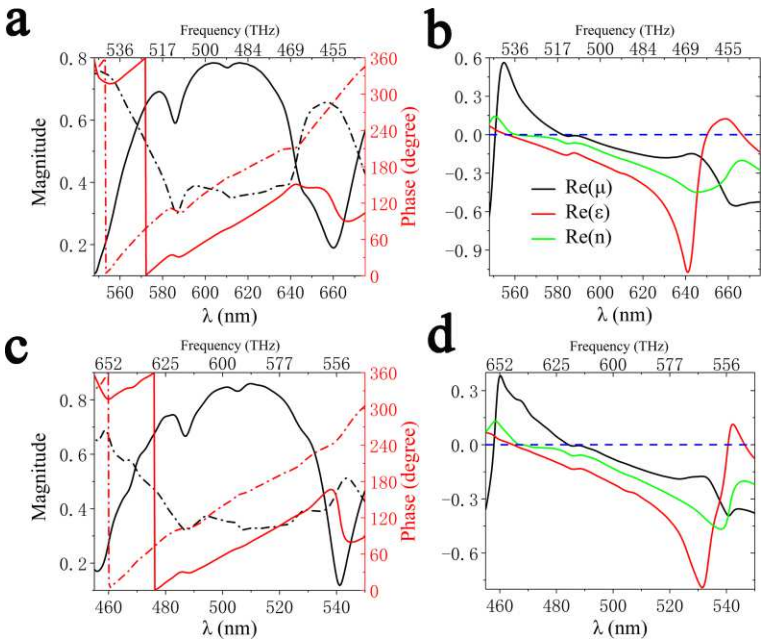

Extended Data Fig. 1 | Numerical simulation of the meta-cluster structure. a, Transmission (solid line) and reflection (dot-dash line) coefficient for the red-light meta-cluster with l = 640 nm, r = 215 nm, and P = 670 nm. **b**, The effective parameters for the red-light meta-cluster retrieved from the coefficients in **a**. **c**, Transmission (solid line) and reflection (dot-dash line) coefficient for the green-light meta-cluster with l = 530 nm, r = 165 nm, and P = 560 nm. **d**, The effective parameters for the green-light meta-cluster retrieved from the coefficients in **c**.

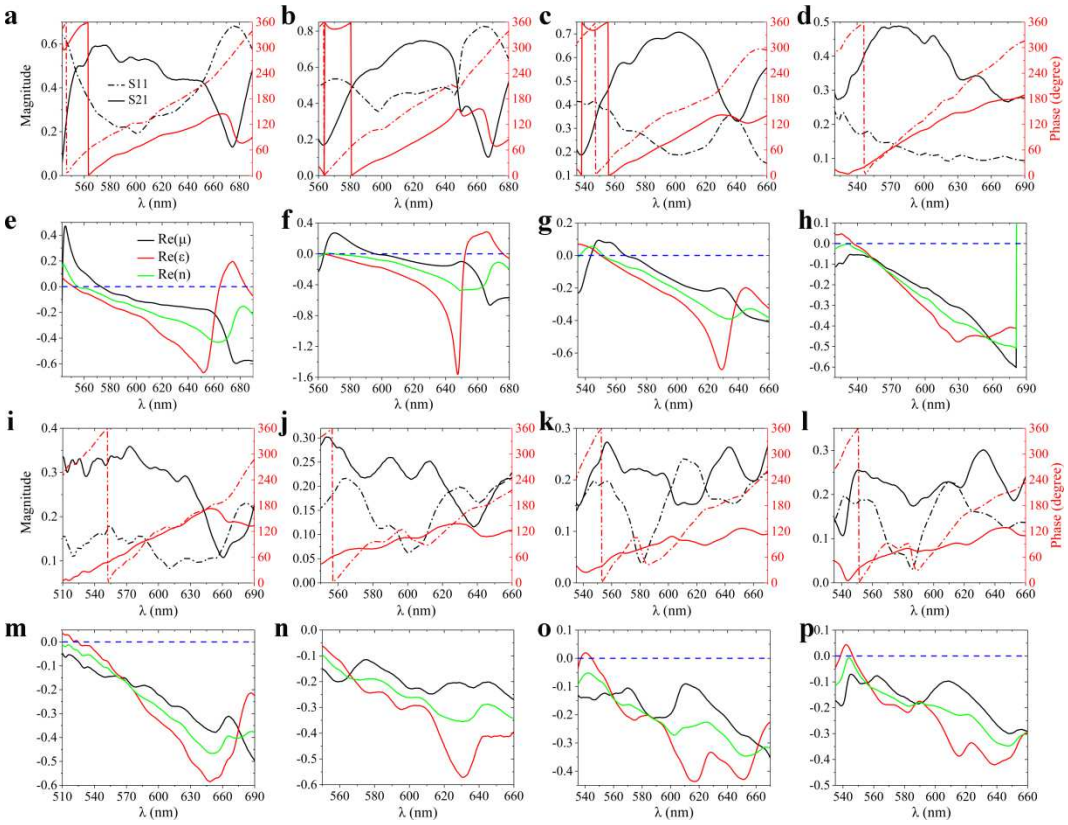

Extended Data Fig. 2 | Effect of Ag layer thickness t_{Ag} on the response behavior of the red-light meta-cluster in PMMA medium. a, **b**, **c**, **d**, Transmission and reflection coefficient curves of the meta-clusters with t_{Ag} = 0.5, 0.7, 2, and 3 nm respectively. **e**, **f**, **g**, **h**, Permeability, permittivity, and refractive index curves of the meta-clusters retrieved from **a**, **b**, **c**, and **d**, respectively. **i**, **j**, **k**, **l**, Transmission and reflection coefficient curves of the meta-clusters with t_{Ag} = 4, 5, 6, and 7 nm respectively. **m**, **n**, **o**, **p**, Permeability, permittivity, and refractive index curves of the meta-clusters retrieved from **i**, **j**, **k**, and **l**, respectively.

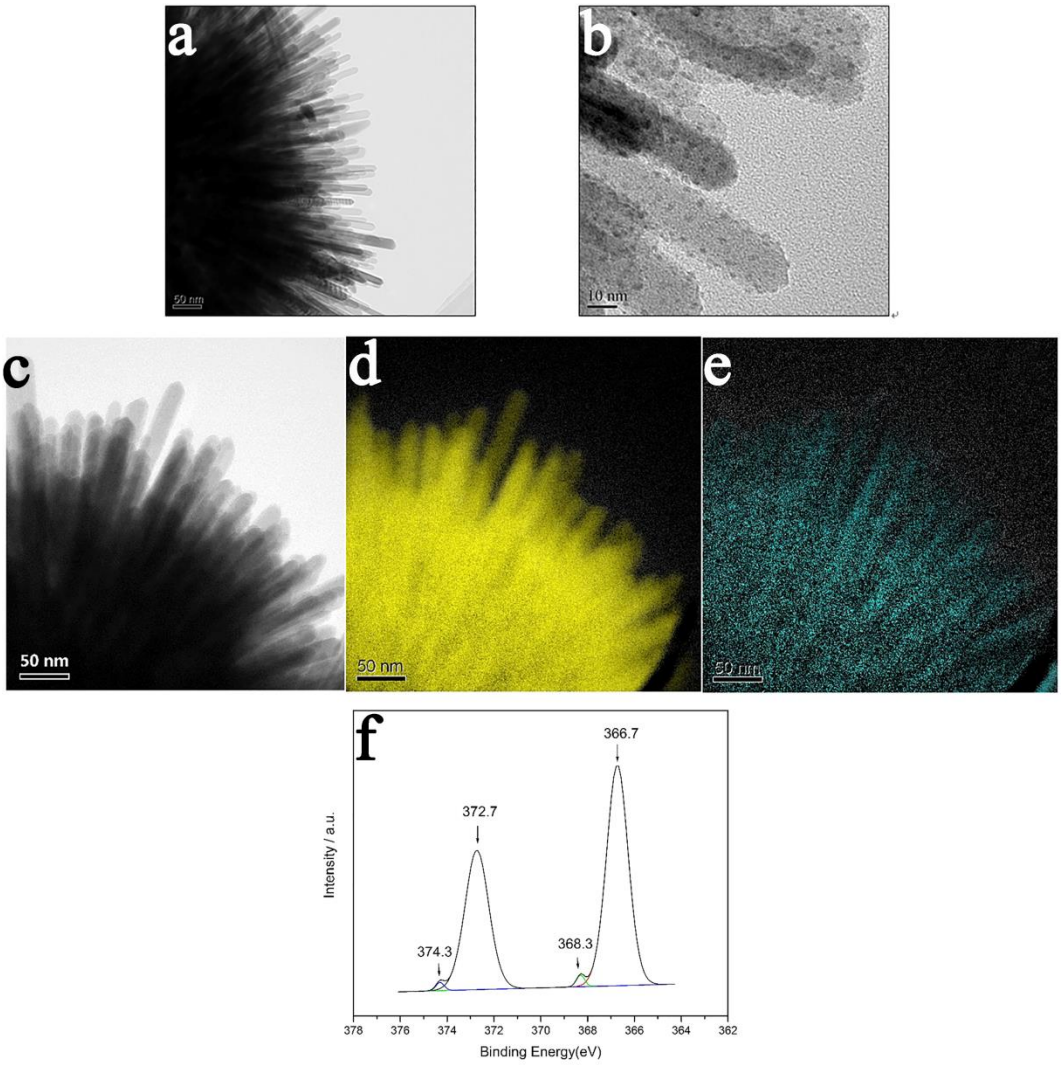

Extended Data Fig. 3 | Characterization of the ball-thorn-shaped composite particle. a, **b**, Local HAADF-STEM images of the Ag/AgCl/TiO_2 particles. **c**, TEM image of Ag/AgCl/TiO_2 particle; **d**, **e**, the corresponding elemental mapping of Ti and Ag, respectively. **f**, XPS analysis of Ag 3d in Ag/AgCl/TiO_2@PMMA.

Extended Data Table 1 | Method and performance comparison of visible metamaterials

Method	Principle	Structure	Size	Min (n')	Max (FOM)	Refs
Direct measurement	Measurements of the refractive index of these structures were performed by observing the refraction angle of light passing through the prism by Snell's law[11].	Meta-cluster composite particles	t_{Ag}=1 nm, D_{rod}=15 nm, L =530/640 nm; R_{core}=165/215 nm	-0.3 (532 nm); -0.41 (630 nm)	4.3 (532 nm); 12.8 (630 nm)	Our work
		cascaded 'fishnet' structures	t_{Ag}=30 nm, Period: 860 nm, t_{MgF2}=50 nm	-1.23 (1775 nm)	3.5 (1775 nm)	13
	A slit was illuminated by a collimated diode laser beam at different incident angles, and the transmitted light was mapped by scanning a tapered optical fiber at the bottom surface of the metamaterial[21].	silver nanowires	Diameter: 60 nm Period: 110 nm	-4 (780 nm)		21
Indirect measurement	The good agreement between the spectroscopic measurements and the numerical simulation indicates the validity of the numerical model. Therefore, the effective refractive index is calculated using the numerical results and a standard retrieval procedure[33].	'fishnet' structures	t_{Ag}=40 nm, Period: 300 nm, t_{MgF2}=17 nm	-0.6 (780 nm)	0.5 (780 nm)	16
		'fishnet' structures	t_{Ag}=33 nm, Period: 300 nm, t_{Al2O3}=38 nm	-1 (776 nm)	0.7 (772 nm)	34
		'fishnet' structures	t_{Ag}=43 nm, Period: 220 nm, t_{Al2O3}=45 nm	-0.25 (580 nm)	0.3 (580 nm)	14
		'fishnet' structures (incorporate gain media)	t_{Ag}=50 nm, Period: 280 nm, t_{Al2O3}=50 nm	-1.26 (738 nm)	10^6 (738 nm)	33
		Multilayered 'fishnet' structures	t_{Ag}=35 nm, Period: 400 nm, t_{HSQ}=15 nm	-1.3 (752 nm)	3.3 (734 nm)	35
		Multilayered 'fishnet' structures	t_{Ag}=22 nm, Period: 240 nm, t_{MgF2}=15 nm	-0.76 (532 nm)	0.5 (532 nm)	17
		'fishnet' structures	t_{Au}=45 nm, Period: 200 nm, t_{air}=15 nm	-1.2 (700 nm)	0.5 (700 nm)	20
	The refractive index and permeability are retrieved from measured reflection and transmission coefficients using walk-off interferometer[38].	Arrays of silver nanorods	Diameter: 80 nm Length: 650 nm	-0.595 (532 nm); -0.629 (639 nm); -0.899 (690 nm)	2.8 (532 nm); 0.5 (639 nm); 0.8 (690 nm)	36

Figures

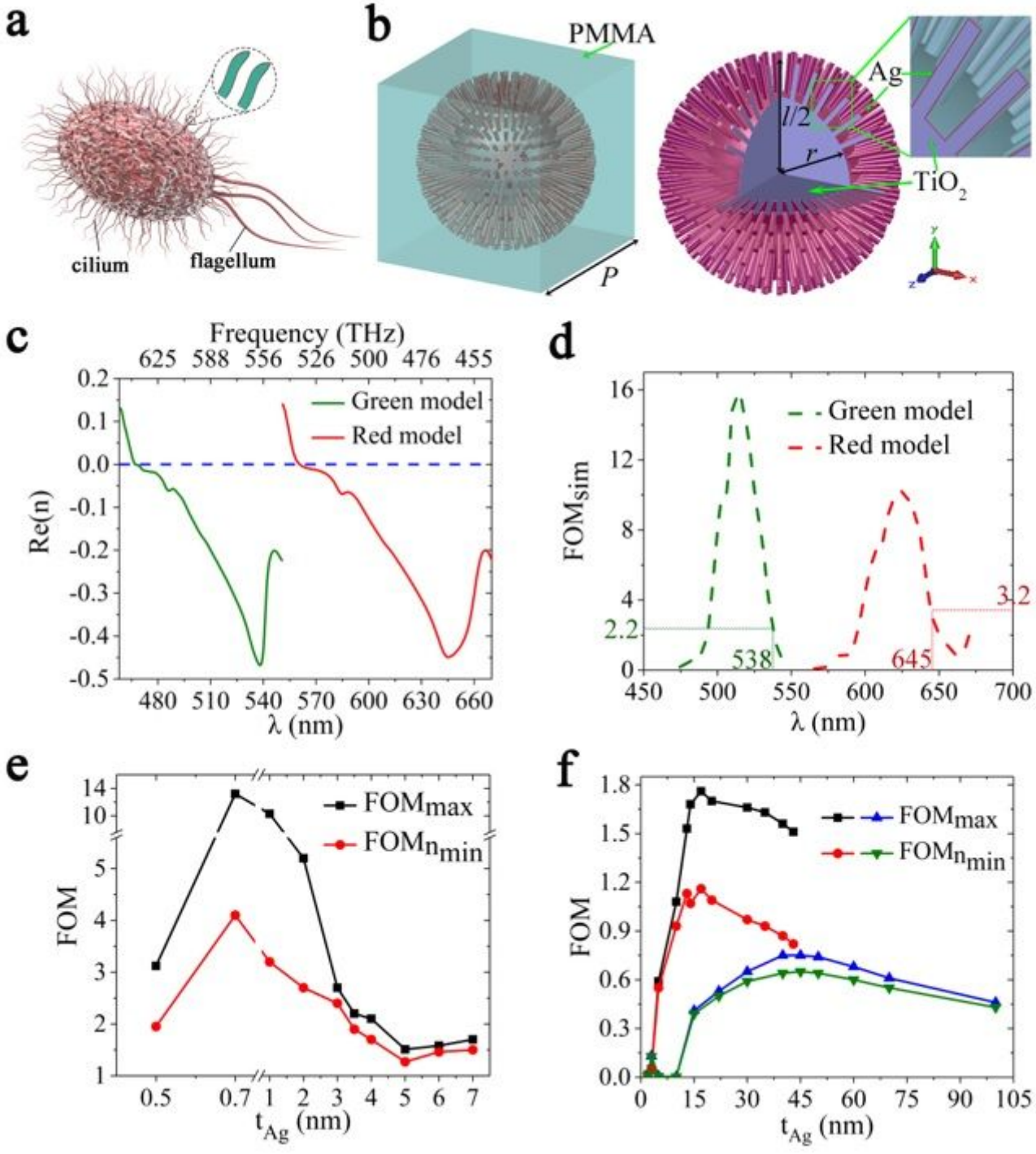

Figure 1

Behavior of the meta-cluster structure. a, Schematic of the biological cilium-cell. b, A meta-cluster model that mimics the cilium-cell structure consisting of a spherical kernel and lots of protruding rods. c, Effective refractive indices for the red-light meta-cluster (red line) with l = 640 nm, r = 215 nm, and P = 670

nm and the green-light meta-cluster (green line) with l = 530 nm, r = 165 nm, and P = 560 nm. d, FOM curves of the meta-clusters resonating at the red-light (red dotted line) and green-light (green dotted line), respectively. e, FOM of the red-light meta-cluster structure as a function of Ag layer thickness tAg. f, FOMs of fishnet structures at different Ag layer thickness. Black square and red circle lines represents the results obtained using the Ag-Al2O3-Ag fishnet structure whose geometrical parameters refer to the published work14 and blue triangle and green inverted-triangle lines represents the results obtained using the Ag-MgF2-Ag fishnet structure whose geometrical parameters refer to the published work17.

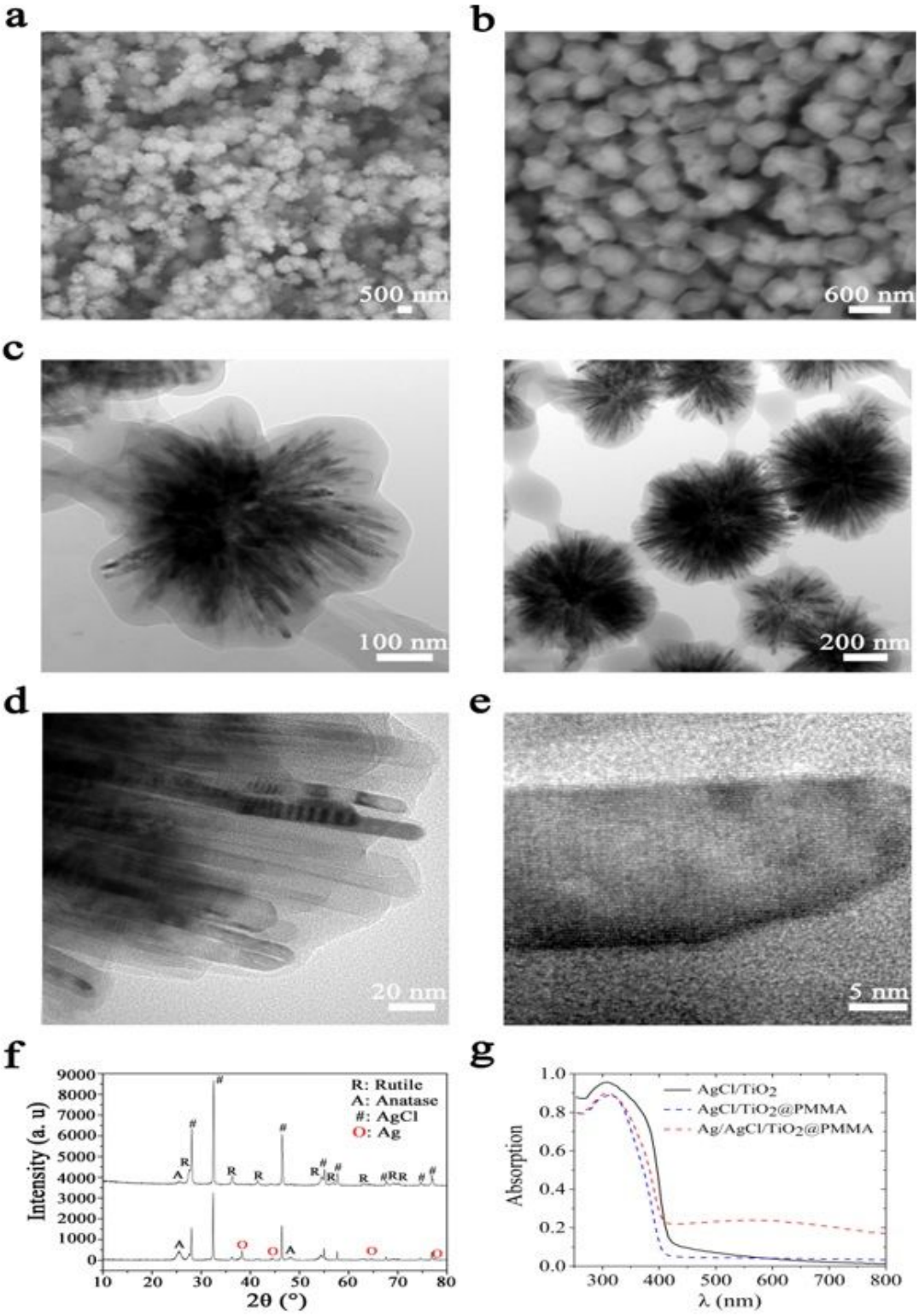

Figure 2

Morphology and characterization of the Ag/AgCl/TiO2@PMMA particles. SEM images of AgCl/TiO2 particles a, Ag/AgCl/TiO2@PMMA particles b. c, d, TEM images of Ag/AgCl/TiO2@PMMA particles: c, field of view of green-light (left) and red-light (right) particles; d, regional view of a composite particle, which is made of a ball-thorn-shaped inorganic kernel and a thin transparent organic PMMA shell. e, A high magnification TEM image of a protruding nanorod, Color variation indicates different chemical compositions. f, XRD patterns of the AgCl/TiO2@PMMA (top) and Ag/AgCl/TiO2@PMMA (bottom) particles. After the particles being photoreduction, in addition to the peaks associated with TiO2 and AgCl crystals, local maximums of varying intensities (red hollow circles) at 38.3°, 44.4°, 64.6°, and 77.5°—corresponding to the respective (111), (200), (220), and (311) crystal faces of Ag—appeared in the bottom spectral line. g, UV-VIS-NIR absorption spectra of AgCl/TiO2 (solid black line), AgCl/TiO2@PMMA (blue dashed line) and Ag/AgCl/TiO2@PMMA particles (red dashed line).

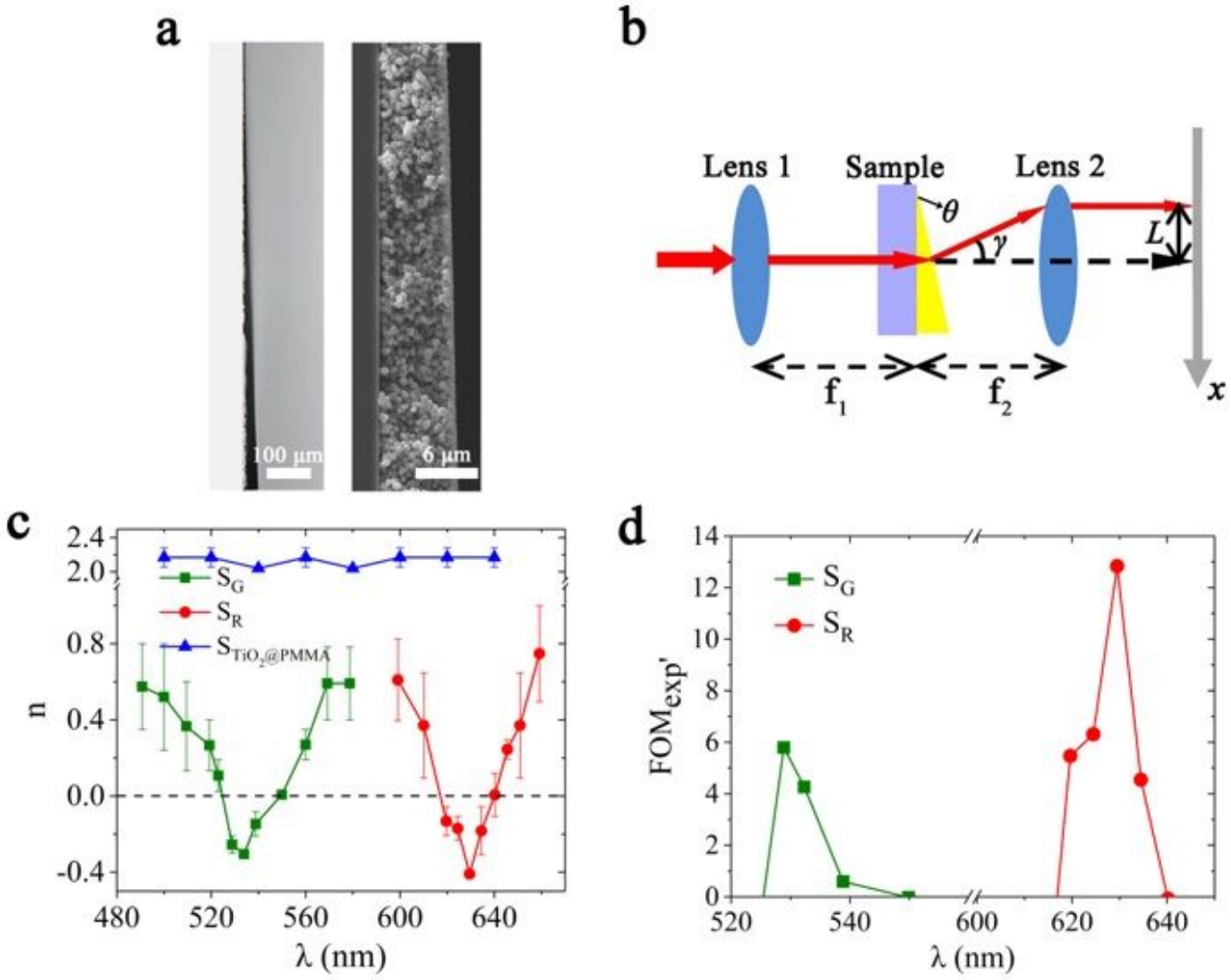

Figure 3

Characterization and measurement of the 3D wedge-shaped samples. a, Microscopic (left) and SEM (right) images of the wedge-shaped metamaterial sample (side view). b, Schematic of negative refraction measurement. θ represents the wedge angle of the prepared 3D wedge-shaped sample. γ refers to the angle between the outgoing beam and the extension line of the incoming beam. L represents the offset of the refracted spot in x-axis. f1 = f2 = 12.7 mm are the focal lengths of lenses 1 and 2, respectively. c, Measured refractive indices of the green-light sample G, the red-light sample R, and the control sample assembled by TiO2@PMMA particles. d, FOMexp' curves of samples G and R at green-light and red-light wavelengths, respectively.

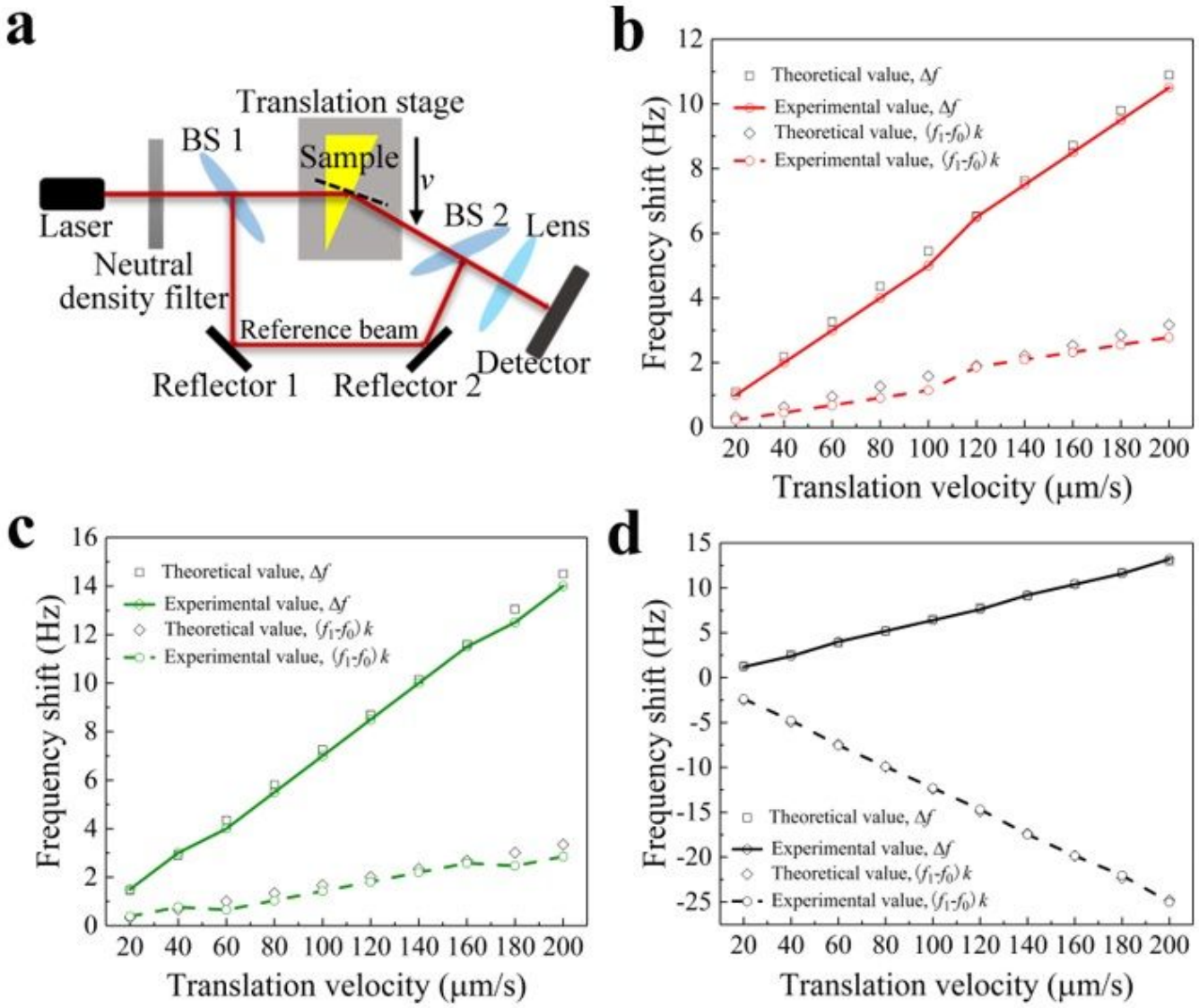

Figure 4

Doppler effect measurement. a, Schematic diagram of Doppler effect heterodyne detection system. b, c, d, Beat frequency and Doppler frequency shift (f1 - f0)k of Doppler effect observed at different velocities for sample Rc, sample Gc, and TiO2@PMMA sample, respectively.

Supplementary Files

This is a list of supplementary files associated with this preprint. Click to download.

- SupplementaryInformation2021.3.4.docx